Single Myosin Lever Arm Orientation in a Muscle Fiber Detected with Photoactivatable GFP[†]

Thomas P. Burghardt,*[,‡,§] Jinhui Li,[‡] and Katalin Ajtai[‡]

Biochemistry and Molecular Biology and Physiology and Biomedical Engineering, Mayo Clinic College of Medicine, Rochester, Minnesota 55905

Received September 16, 2008; Revised Manuscript Received November 3, 2008

ABSTRACT: Myosin 2 is the molecular motor in muscle. It binds actin and executes a power stroke by rotating its lever arm through an angle of ~70° to translate actin against resistive force. Myosin 2 has evolved to function optimally under crowded conditions where rates and equilibria of macromolecular reactions undergo major shifts relative to those measured in dilute solution. Hence, an important research objective is to detect in situ the lever arm orientation. Single-molecule measurements are preferred because they clarify ambiguities that are unavoidable with ensemble measurements; however, detecting single molecules in the condensed tissue medium where the myosin concentration exceeds 100 μM is challenging. A myosin light chain (MLC) tagged with photoactivatable green fluorescent protein (PAGFP) was constructed. The recombinant MLC physically and functionally replaced native MLC on the myosin lever arm in a permeabilized skeletal muscle fiber. Probe illumination volume was minimized using total internal reflection fluorescence microscopy, and PAGFP was sparsely photoactivated such that polarized fluorescence identified a single probe orientation. Several physiological states of the muscle fiber were characterized, revealing two distinct orientation populations in all states called straight and bent conformations. Conformation occupancy probability varies among fiber states with rigor and isometric contraction at extremes where straight and bent conformations predominate, respectively. Comparison to previous work on single rigor cross-bridges at the A-band periphery where the myosin concentration is low suggests molecular crowding in the A-band promotes occupancy of the straight myosin conformation [Burghardt, T. P., et al. (2007) *Biophys. J. 93*, 2226]. The latter may have a role in contraction because it provides additional free energy favoring completion of the cross-bridge power stroke.

Myosin 2 is the actin-dependent molecular motor driving sarcomeric shorting and muscle contraction by transducing chemical free energy from MgATP hydrolysis into directed movement (*1, 2*). The MgATP hydrolysis is coupled to a series of conformational changes in myosin, resulting in a cycle of attachment to the actin filament, strain development, release, and reattachment. Myosin structural intermediates from the cycle summarized in Scheme 1 were uniquely identified by near-ultraviolet circular dichroism spectra and nucleotide sensitive tryptophan fluorescence intensity changes (*3*).

In the absence of actin (A) at steady state, myosin transient intermediate states M, M*, M**, and M^ are occupied at fractional concentrations known for several different myosins (*3*−*5*). Work production begins in Scheme 1 with actin binding to M** followed by an ordered release of products (first P_i and then ADP) while the lever arm rotates to impel actin (*2*).

Myosin heavy chain (MHC)[1] is a linear molecule ~170 nm in length consisting of three distinct regions: an N-terminal head domain, a neck region containing one or more IQ domains binding light chains, and a C-terminal tail responsible for heavy chain dimerization. The globular N-terminus, containing the active site for MgATPase and the actin binding site, forms cross-bridges with actin filaments in muscle fibers to generate contractile force. The head domain is called subfragment 1 (S1) when cleaved from myosin by proteolysis. The ~160 nm C-terminal tail forms a coiled coil dimer that further assembles into the multimeric thick filaments in the A-bands of the muscle fiber sarcomere. Myosin light chains arranged in tandem in the head−tail junction form a stabilizing collar around the heavy chain α-helical neck thought to function as the lever arm (*6, 7*). Each light chain binds to a so-called IQ motif, a loosely conserved sequence with the consensus $IQX_3RGX_{3-4}R$, where X can be any amino acid.

Atomic structures of S1 suggested that small conformational changes in the active site induced by ATP hydrolysis are amplified to the large linear displacements by lever arm

[†] This work was supported by NIH-NIAMS Grant R01AR049277 and the Mayo Foundation.

* To whom correspondence should be addressed. Telephone: (507) 284-8120. Fax: (507) 284-9349. E-mail: burghardt@mayo.edu.

[‡] Biochemistry and Molecular Biology.

[§] Physiology and Biomedical Engineering.

[1] Abbreviations: GFP, green fluorescent protein; HCRLC, human cardiac myosin regulatory light chain; KPr, potassium propionate; MHC, myosin heavy chain; MLC, myosin light chain; NA, numerical aperture; PAGFP, photoactivatable GFP; PALM, photoactivated localization microscopy; PsA, photoselected activation; PSF, point spread function; RLC, myosin regulatory light chain; S1, myosin subfragment 1; TFP, trifluoroperazine; TIRF, total internal reflection fluorescence; WT, wild type.

10.1021/bi8017703 CCC: $40.75
Published on Web 01/07/2009

Scheme 1

$$\begin{array}{ccccccc} AM+ATP \leftrightarrow & AM^{*}\cdot ATP & \leftrightarrow & AM^{**}\cdot ADP\cdot P_i & \leftrightarrow & AM^{\wedge}\cdot ADP+P_i & \leftrightarrow AM+ADP+P_i \\ & \updownarrow A & & \updownarrow A & & & \\ & M^{*}\cdot ATP & \leftrightarrow & M^{**}\cdot ADP\cdot P_i & & & \end{array}$$

rotation (*8*). The idea is consistent with early experiments showing rotary motion within S1 (*9*−*11*) and with experiments showing correlation between lever arm length and in vitro velocity (*12*). S1 crystal structures showed that the lever arm assumed different orientations in the absence (*13*) and presence (*6*) of nucleotides and that the apparent rotation carries bound MLCs through the identical rotational trajectory while their conformations are approximately unchanged. MLC location and exchangeability (*14*) are exploited in the study of lever arm conformation.

An orientation sensitive spin probe was introduced into the lever arm by modification of an isolated MLC that was then reintroduced into the muscle by light chain exchange (*15*). Genetically engineered MLCs containing a single cysteine selectively modified at the SH group by a fluorescent probe were likewise introduced into the muscle with light chain exchange. Labeled MLC dynamics in muscle fibers was detected with time-resolved fluorescence polarization indicating lever arm rotational movement during contraction (*16*). More recently, fluorescently labeled RLC and ELC were simultaneously exchanged into fibers (*17*). We performed MLC exchange with GFP-tagged MLC (*18*). The GFP fluorescent reporter group for lever arm rotation accomplishes in situ single-molecule isolation and translates to in vivo applications (*18, 19*), surpassing organic probe capabilities.

Wild-type GFP has two long-wavelength absorption bands at ∼400 and 480 nm with emission at ∼510 nm (*20*). The 400 and 480 nm absorption peaks correspond to mixed populations of neutral phenols and anionic phenolates at Tyr66, respectively (*21*). PAGFP is the T203H substitution variant with the 400 nm absorption band preferentially stabilized (*22*). PAGFP has little fluorescence under 488 nm excitation until photoactivated by irradiation in its 400 nm band. Photoactivation causes a 100-fold increase in fluorescence excited by 488 nm light. Photoactivated PAGFPs remain in the activated conformation for weeks.

Photoactivated localization microscopy (PALM) (*23, 24*) uses PAGFP or other photoactivatable fluorescent proteins (PA-FPs) to accomplish ∼10 nm spatial resolution microscopy. PA-FP's tagged target proteins produced in cells where they assemble into structures at high density. Photoactivation produced a sparse concentration of fluorescent species that were continuously illuminated and individually imaged until they were photobleached. The single PA-FP image was then localized to higher precision than the diffraction resolution limit by determining its center of fluorescence emission by fitting the point spread function (PSF) to its measured photon distribution. Fluorescent dyes Cy5 (primary) and Cy3 (secondary) are configured to form a photoactivatable switch replacing PAGFP in a technique analogous to PALM called stochastic optical reconstruction microscopy (STORM) (*25*). The Cy5−Cy5 switch is smaller than PAGFP, making it an appropriate choice in some applications.

Optical microscopic characterization of proteins in a biological assembly provides structural and dynamical information sometimes accumulated as ensemble-averaged signals. Alternatively, emerging single-molecule techniques clarify averaging ambiguities unavoidable with ensemble measurement (*26*). Measurements from single-motor proteins in vitro are preferred for characterization of motor function, yet it does not represent the native system in a cell where molecular crowding is the norm (*27*). Under physiological conditions, crowding contributes substantially to the total free energy of the muscle fiber. It causes major shifts in the rates and equilibria of macromolecular reactions relative to those measured in dilute (probably in vitro) conditions. Myosin 2 has evolved to function optimally under crowded conditions; hence, observing its native behavior depends upon the maintenance of the native environment. A crowded environment produces preferential hydration of a protein, thereby favoring lower-surface area structures and promoting self-association. This phenomenon was observed in skeletal muscle myosin (*28*), suggesting that in situ and in vitro single molecules could differ functionally or structurally.

In previous work, human cardiac ventricular RLC (HCRLC) was tagged with GFP at the C-terminus (HCRLC-GFP) and exchanged into a permeabilized skeletal muscle fiber (*18*). Exchanged fibers retained their native ability to develop isometric force. GFP fluorescence in exchanged fibers was confined to the A-band, indicating association with the myosin lever arm. HCRLC-GFP-exchanged fiber images had pixels containing one to six or at least seven GFPs that were distinguished by a quantized change in fluorescence intensity per pixel versus photon count threshold. Pixels containing single molecules were at the A-band periphery where the myosin concentration drops to zero from its peak value of 120−300 μM within the A-band (*29, 30*). Pixels containing two or more GFPs were distributed closer to the A-band center. Single-GFP fluorescence polarization at the A-band periphery differed significantly from ensemble probe fluorescence polarization within the A-band.

In this work, photoactivatable GFP-tagged HCRLC (HCRLC-PAGFP) was exchanged with the native light chain on myosin cross-bridges in permeabilized skeletal muscle fibers. Sparse photoactivation of the PAGFP permitted detection of single cross-bridge lever arm orientation across the entire A-band. We found that single myosin lever arms have two conformation populations with different average dipole orientations but that the two conformations are identifiable in rigor, with MgADP bound, relaxation (normal and low ionic strengths), and isometric contraction. Characteristic of each physiological state are the occupation probabilities for the distinct lever arm orientation populations. The single-molecule analysis gives a detailed assessment of a fundamental lever arm characteristic under the native crowded conditions.

MATERIALS AND METHODS

Chemicals. ATP, sodium azide, dithiothreitol (DTT), phenylmethanesulfonyl fluoride (PMSF), porcine troponin, and P^1,P^5-di(adenosine-5′)pentaphosphate (Ap_5A) were from Sigma (St. Louis, MO). The Bradford protein concentration assay was from Bio-Rad (Hercules, CA). SYPRO Ruby fluorescent stain and rhodamine-labeled phalloidin were from Invitrogen (Carlsbad, CA). Rabbit troponin C was from Life Diagnostics (West Chester, PA). Leupeptin, chymostatin, and pepstatin were from Roche Applied Sciences (Indianapolis, IN).

GFP- and PAGFP-Tagged HCRLC Construction. The cDNA of wild-type HCRLC cloned into pET-3d (Novagen) plasmid vectors was a generous gift from D. Szczesna-Cordary (University of Miami, Miami, FL) (*31*). The HCRLC C-terminus was modified with the peptide GGGG-GGVPVEK-GFP (HCRLC-GFP) and then constructed and purified as described previously (*18*). Conversion of GFP to a photoactivatable form (PAGFP) occurred with the T203H and V163A substitutions (*22*) generated in GFP using Quickchange site-directed mutagenesis (Stratagene, La Jolla, CA). The T203H substitution converts the chromophore to the photoactivatable form, while the V163A substitution enhances folding kinetics. Primers for the V163A mutation were 5′-GAATGGAATCAAAGCTAACTTCAAAATTAG-3′ and 5′-CTAATTTTGAAGTTAGCTTTGATTCCATTC-3′. Primers for the T203H mutation were 5′-GACAACCAT-TACCTGTCCCACCAATCTGCCCTTTCG-3′ and 5′-GGGCAGATTGGTGGGACAGGTAATGG-3′.

Fiber Preparation and Light Chain Exchange. Rigor, Relax, Active, and other solutions used are listed in Table 1 of ref *18*, where all ionic strengths are 150−160 mM. We also used an ADP and a low-ionic strength (low-μ) Relax solution. The ADP solution is the Relax solution with 4 mM ADP replacing ATP, 0.1 mM Ap_5A, and with an ionic strength comparable to that of the Relax solution. The low-μ Relax solution is the Relax solution except with 10 mM imidazole, 2 mM EGTA, 2 mM ATP, 2 mM magnesium acetate, no potassium propionate (KPr), and an ionic strength of ∼27 mM.

Rabbit psoas muscle fibers were obtained as described previously (*32*) and kept in bundles of 100−200 fibers in Glycerinating solution [Relax solution containing 50% glycerol (pH 7)] at −20 °C and stored for up to several weeks.

Exchange of HCRCL or HCRLC-GFP into single rabbit psoas muscle fibers was described previously (*18*). The approach is to remove native RLC with an extracting solution at 30 °C containing EDTA chelating the Mg^{2+} stabilizing binding of RLC to myosin and to replace it with the exogenous protein. Troponins extracted by this treatment are reconstituted. Light chain exchange efficiency was measured by detecting loss of native RLC and replacement with HCRLC-GFP by SDS−PAGE on proteins extracted from the muscle fibers (*18*). All experiments utilized an exchange fraction of 60−70%.

HCRLC-GFP was localized to the A-band of the muscle fiber using TIRF microscopy. Figure 1s (top) of the Supporting Information shows GFP fluorescence intensity from a HCRLC-GPF-exchanged fiber plotted versus length along the sacromere. Intensity modulation follows the expected A-band length and shows a dip at the M-line where there are no myosin cross-bridges. The HCRLC-GPF-exchanged fiber was then incubated with rhodamine-labeled phalloidin (Rh-phalloidin). The Rh-phalloidin binds F-actin and localizes to the overlap zone where thick and thin filaments overlap and to the I-band. The doubly labeled fiber was fluorescence imaged under conditions favoring GFP or rhodamine emission. Figure 1s (bottom) of the Supporting Information shows the two images merged. The colors separate into red (Rh-phalloidin) and green/red (HCRLC-GFP/Rh-phalloidin) bands indicating the I-band and overlap zone, respectively. Results are equivalent to those of Rh-skeletal-RLC-exchanged muscle fibers (*33*).

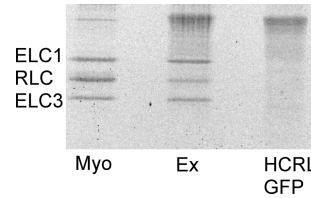

FIGURE 1: Low-molecular weight portion of a SDS−PAGE gel containing myosin. Skeletal myosin (Myo), TFP-extracted native RLC and exchanged HCRCL-GFP myosin (EX), and purified HCRLC-GFP are in the gel stained with SYPRO Ruby. Gel scanning indicates exogoneous HCRLC-GFP replaces 60% of the native RLC with a 1:1 stoichiometry.

Tension measurements were performed on control and exchanged single muscle fibers to investigate how HCRLC or HCRLC-GFP substitution affects contractility (*18*). Exchange of the light chain followed by troponin reconstitution restores 87 and 81% of control contractility for HCRLC and HCRLC-GFP, respectively. Results are equivalent to those of Rh-skeletal-RLC-exchanged muscle fibers (*33*).

In Vitro Light Chain Exchange into Myosin. We used trifluoroperazine (TFP) to exchange HCRLC-GFP into full-length skeletal myosin using an established protocol (*34*). Figure 1 shows native myosin (MYO), exchanged myosin (EX), and purified HCRLC-GFP in the light chain-containing region of a SDS−PAGE gel stained with SYPRO Ruby. Quantitative gel scanning using ImageJ indicated exogoneous HCRLC-GFP replaces 60% of the native RLC with a 1:1 stoichiometry.

Spectroscopic measurements on HCRLC-GFP, HCRLC-PAGFP, and HCRLC-GFP-exchanged myosin were conducted under conditions exactly imitating those for the fiber experiments with Apo∼Rigor, +ATP∼Relax, +ATP+Ca∼Active, +ADP∼ADP, and +ATP(L)∼low-μ Relax. High-ionic strength (H) conditions, needed for experiments with full-length skeletal myosin, implied addition of KPr or KCl to a final concentration of 0.5 M, giving an ionic strength of ∼580 mM. We observed no spectroscopic difference between measurements taken under high-ionic strength conditions using KPr or KCl. Other in vitro conditions not duplicated in the fiber experiments are low-μ Apo and +Ca. The low-μ Apo condition, Apo(L), is the +ATP(L) condition without ATP, and +Ca implied addition of 0.1 mM $CaCl_2$ to the Apo condition (normal or high ionic strength).

Total Internal Reflection Fluorescence (TIRF) Polarization Microscopy. The inverted microscope setup was described in detail previously (*18*). Excitation light (488 nm) from an argon ion laser was focused on the back focal plane of a 1.45 numerical aperture (NA) objective and incident from the glass side of a glass−water interface at angles greater than the critical angle for total internal reflection (TIR). Although light is totally reflected, an evanescent field created in the water medium and decaying exponentially with distance from the interface excites fluorophores within ∼100 nm of the surface (*35*). Polarized electric field intensities for the evanescent field were shown previously (*18*). The p-polarized incident light has electric field polarization in the incidence plane and produces an elliptically polarized evanescent electric field. Evanescent intensity is predominantly polarized normal to the interface (*36*). The s-polarized

incident light has electric field polarization perpendicular to the incidence plane that is continuous across the interface.

A HCRLC-PAGFP-exchanged muscle fiber in aqueous buffer solution makes contact with the TIR-supporting glass substrate and is illuminated by the evanescent field. Excited fluorescence collected by the objective is spectrally filtered and formed into an image by the microscope (Olympus IX71) tube lens at a plane within a polarizing beam splitter (DualView, MAG Biosystems, Pleasanton, CA). The beam splitter separates emitted light into two linear polarizations that are reimaged on two halves of the light sensitive area of the 12 bit CCD camera (Hamamatsu Orca ER). Pixel size (6.45 μm) together with the evanescent field depth defines a minimum object space detection volume of $\sim 2 \times 10^6$ nm^3 for the 60× objective (*37*). The detection volume contains ~150−370 RLCs near the A-band center (*29, 30*) except at the M-line borders where the cross-bridge is excluded.

In most cases, sparse PAGFP photoactivation was accomplished under TIR using a 10−20 s exposure to 488 nm light from the argon ion laser. The laser intensity was ~10−100-fold higher during photoactivation compared to that used during fluorescence excitation of photoactivated PAGFPs. An alternative excitation light pathway causing dense PAGFP photoactivation had a 100 W Hg arc lamp illuminating an ~20 μm diameter circular disk on the sample. Infrared and band-pass filters in the Hg lamp pathway transmitted light wavelengths of 410 ± 20 nm. The 410 nm light transmits the sample (unlike the TIR laser excitation light).

Microscopic fluorescence polarization contains polarization selective absorption and emission effects both contributing to the sensitivity of the signal to orientation of the emitting dipole. Fluorescence polarization is expressed as ratios to eliminate the dependence on absolute intensities such that

$$P_{||} = \frac{F_{||,||} - F_{||,\perp}}{F_{||,||} + F_{||,\perp}} \quad P_{\perp} = \frac{F_{\perp,\perp} - F_{\perp,||}}{F_{\perp,\perp} + F_{\perp,||}} \tag{1}$$

where $F_{i,j}$ is fluorescence intensity for incident excitation electric field polarization i and fluorescence emission electric field polarization j. For a muscle fiber, || (parallel) or ⊥ (perpendicular) means relative to the fiber symmetry axis. The p-polarized incident TIR light produced the ⊥ excitation in eq 1 with an evanescent field that is predominantly perpendicular to both orientations of the emission polarization analyzer. This is unlike epi-illumination fluorescence polarization where exciting light polarization is never perpendicular to both orientations of the emission polarization analyzer. Collected frames contained || and ⊥ polarization-emitted light images combined pixel by pixel into the ratios in eq 1. Single-molecule images occupied a 2 × 2 pixel region due to the objective PSF. Pixels in collected images were binned 2 × 2 (effective pixel size of 12.9 μm) before polarization ratios were computed.

The proximity of the TIR interface affects probe emission properties (*38, 39*). Data analysis manages both the perturbing effect of the TIR interface on probe emission and the effect of high-NA collection of light, known to impair the ability to resolve emitter dipole components using an analyzing polarizer (*18, 40*).

Image Analysis. The region occupied by the fiber image is defined by inspection, and a graph is created by plotting local average counts (A) versus total fluorescence (F) in the (i,j)th pixel. The local average count for a pixel at position (i,j) is the average of counts in pixels surrounding (i,j) within a radius approximately corresponding to the size of distinct features in the fiber image (~1 μm). At the low end of the A scale, the A versus F relationship is linear and fitted by linear regression. The slope is 10−20% larger than 1 because fewer pixels containing photoactivated molecules fall in the lower-A range. The fitted line defines the upper half-plane where fluorescence from pixels containing photoactivated molecules should fall. Upper half-plane pixels are rejected from further analysis if their intensity is less than slope x (local average counts + one standard deviation), thereby eliminating most pixels (~94% assuming a Gaussian distribution about the average) containing molecules not photoactivated but falling in the upper half-plane due to noise fluctuation. A pixel containing a photoactivated molecule has its local average background subtracted, and the remaining light is used to compute the fluorescence polarization ratio using eq 1. Emission from a dipole is polarized, but the total fluorescence, F, is independent of dipole orientation. We approximate F from dipoles in the fiber with unknown orientation, for the purpose of identifying photoactivated PAGFPs, by using the relationship $F = F_{||,||} + 2F_{||,\perp}$ or $F = F_{\perp,\perp} + 2F_{\perp,||}$.

Polarized PAGFP photoactivation affects the polarization ratios because of photoselection. $P_{||}$ or $P_{\perp}$ ratios shown here are from probes photoactivated with light polarized parallel or perpendicular to the fiber axis and measured from different regions of the fiber. Alternative combinations of photoactivation and emission polarization are also suitable for analysis but were not used here.

Activated Fluorescence Polarization. Irreversible isomerization, $N_B \rightarrow N_A$, where the total number of molecules (N) is the sum of the number of molecules of unphotoactivated (N_B) and photoactivated (N_A) species, describes fluorescence photoactivation. Solving for $N_A(t)$,

$$N_A = N[1 - \exp(-k_A t_A)] \approx N k_A t_A \tag{2}$$

where k_A is the activation rate, t_A is the activating light pulse duration, and the approximation is for sparse photoactivation where $k_A t_A \ll 1$. The absorption cross section is proportional to $(\mu_a \cdot \mathbf{E})^2$; hence, $k_A t_A \propto (\mu_a[B] \cdot \mathbf{E})^2$, where $\mu_a[B]$ is the absorption dipole moment for the unphotoactivated species and $\mathbf{E}$ is the activating light electric field polarization vector. For single molecule i, the normalized probability for its photoactivation, $\gamma_{A,i}$, is

$$\gamma_{A,i} = \frac{(\mu_{aj}[B] \cdot \mathbf{E})^2}{\sum_{j=1}^{N} (\mu_{a,j}[B] \cdot \mathbf{E})^2} \tag{3}$$

In the simulation, a random number, θ, between 0 and 1 is compared to $\gamma_{A,i}$. If $\theta < \gamma_{A,i}$, molecule i is photoactivated. Photoactivated molecule polarized fluorescence, F_i, is computed with

$$F_i = (\mu_{a,i}[A] \cdot \mathbf{E})^2 (\mu_{e,i}[A] \cdot \nu)^2 \tag{4}$$

where $\mu_{a,i}[A]$ and $\mu_{e,i}[A]$ are the absorption and emission dipole moments, respectively, for the ith molecule of photoactivated species excited in the long-wavelength band

and ν is the emission polarizer orientation. We assume $\mu_{a,i}$[A], $\mu_{a,i}$[B], and $\mu_{e,i}$[A] are aligned to simplify numerical generation of polarization ratio histograms. It is unlikely that $\mu_{a,i}$[A] and $\mu_{a,i}$[B] are precisely aligned. A related fluorescent protein has significant rearrangement of the chromophore orientation in an apparently analogous photoactivation process (*41*). This limitation in the modeling may need to be addressed in future work. We will show in Results that anisotropies are near the theoretical maximum of 0.4, indicating good alignment of $\mu_{a,i}$[A] and $\mu_{e,i}$[A]. Photoactivated PAGFP dipole moments have limiting anisotropy probably exceeding 0.35 corresponding to an angle of <24° between dipoles.

Active isometric and relaxed muscle fiber states have cross-bridge dynamics on a time domain intermediate between the experimental sampling time (seconds) and the fluorescence lifetime (nanoseconds). The dynamics modifies $\gamma_{A,i}$ (eq 3) and F_i (eq 4) by introducing a time average over the solid angular domain visited by the PAGFP and is equivalent to defining an ensemble representing the angular space visited by PAGFP and then ensemble averaging. We will show that both states exhibit substantial orientational ordering, suggesting the lever arm maintains a preferred direction during the observation interval and that the preferred directions do not differ much for the various physiological states of the fiber that have been investigated. It implies that transitions between the observed oriented conformations do not occur with a frequency substantially modifying their orientation characteristics during one observation time interval; hence, we do not introduce dynamics into the data analysis.

Polarization and Dipole Angular Distributions. $P_{||}$ and $P_{\perp}$ ratios from single molecules in permeabilized fibers are indicated by histograms with $-1 \leq P \leq 1$ on the abscissa and molecule count on the ordinate. We estimated dipole orientations simultaneously corresponding to $P_{||}$ and $P_{\perp}$ using a probe dipole orientation Gaussian distributed with mean x_0 and standard deviation σ_x. Then,

$$D(\alpha, \alpha_0, \sigma_\alpha, \beta, \beta_0, \sigma_\beta) = \frac{1}{\sqrt{2\pi\sigma_\alpha^2}} \mathrm{Exp}\left[-\frac{(\alpha-\alpha_0)^2}{2\sigma_\alpha^2}\right] \times \frac{1}{\sqrt{2\pi\sigma_\beta^2}} \mathrm{Exp}\left[-\frac{(\beta-\beta_0)^2}{2\sigma_\beta^2}\right] \quad (5)$$

is the parent distribution for probe dipole orientation with mean azimuthal and polar angles, α_0 and β_0, respectively, measured relative to the fiber axis and distribution widths, σ_α and σ_β. At each grid point (α_0,σ_α,β_0,σ_β), we generated 2500 random values for (α,β) consistent with the parent distribution. The (α,β) pairs were converted into 2500 ($P_{||}$,$P_{\perp}$) pairs using eqs 1, 3, and 4. The ($P_{||}$,$P_{\perp}$) pairs were then converted into theoretical histograms for comparison to data. The grid domain is defined with $0 \leq \alpha_0$, $\sigma_\alpha \leq \pi$, and $0 \leq \beta_0$, $\sigma_\beta \leq \pi/2$. The grid resolution is 15° for α_0 and σ_α or 3° for β_0 and σ_β for $\sim 1.6 \times 10^5$ total grid points. Fluorescence polarization ratios are equal for any combination of α_0, $\alpha_0 + \pi$, β_0, and $\pi - \beta_0$ because the fluorescence intensity originates from an electric transition in the GFP. Thus, grid domain limits on α_0 and β_0 do not affect the generality of the results. Distribution widths limits were decided from experience fitting the data. Theoretical histograms were compared to measured $P_{||}$ and $P_{\perp}$ histograms using the χ^2 test with weights given by the variance of the experimental data. Choices for (α_0,σ_α,β_0,σ_β) corresponded to the lowest χ^2 fits consistent with the *F*-ratio test, where the largest χ^2 allowed is consistent with a random selection of data obeying the correct parent distribution with a probability of >0.05. In some cases, theoretical $P_{||}$ histograms fitted Gaussians approximating the measured $P_{||}$ and $P_{\perp}$ histograms. Then points in the χ^2 test are weighted equally. The *F*-ratio test criterion led to 100−300 selections for (α_0,σ_α,β_0,σ_β) that are statistically consistent with data. This selection set is called the "allowed selections".

RESULTS

Fluorescence Spectroscopy. GFP and PAGFP chromophores are the result of the autocatalytic cyclization of the S65-Y66-G67 polypeptide backbone and oxidation of the $C_\alpha-C_\beta$ bond in Y66 giving a large delocalized π-system. The PAGFP chromophore can photoactivate probably due to substantial rearrangement of the chromophore and vicinal side chains (*41*) facilitated by the T203H substitution (*22*). Fluorescence polarization anisotropy from photoactivated PAGFP-tagged HCRLC exchanged into fibers was interpreted under conditions requiring addition of nucleotides (ADP or ATP), cation (Ca^{2+}), and adjustment of the ionic strength. We studied the effect of these "perturbants" on HCRLC-PAGFP and HCRLC-GFP spectroscopy to surmise how they affect the local and global mobility of the chromophore.

HCRLC-PAGFP-exchanged full-length skeletal myosin is soluble only at a high ionic strength (0.5 M KCl or KPr). The high-ionic strength condition totally quenched photoactivated PAGFP fluorescence but did not elicit a similar response in HCRLC-GFP. A similar concentration of halide ions quenched the fluorescence of an enhanced GFP variant with S65T and T203Y substitutions (*42*). Hence, we investigated the effect of perturbants on PAGFP-tagged myosin photophysics in two steps. In step 1, we measured the effect of the perturbants on the fluorescence polarization anisotropy of HCRLC-GFP alone and when exchanged into full-length skeletal myosin. In step 2, we measured the effect of the perturbants on the fluorescence polarization anisotropy of HCRLC-PAGFP alone. Global structures of GFP and PAGFP are identical; hence, results pertaining to global dynamics of GFP on the surface of full-length myosin can be applied to PAGFP. Local dynamics are measured and compared directly between HCRLC-GFP and HCRLC-PAGFP.

Polarization anisotropy shown in the large panel of Figure 2 is for excitation at 488 ± 6 nm with emission collected through a 40 nm width band-pass filter centered on 550 nm. Error bars show the standard deviation. Conditions exactly imitated those for the fiber experiments with Apo∼Rigor, +ATP∼Relax, +ATP+Ca∼Active, +ADP∼ADP, and +ATP(L)∼low-μ Relax. Conditions defined in Figure 2 and their associated ionic strengths are indicated in Materials and Methods. Polarization anisotropy from HCRLC-GFP in solution (■) varies within the standard deviation over all conditions tested. Polarization anisotropy from HCRLC-PAGFP in solution (□) also varies within the standard deviation over all conditions tested except the Apo(L)

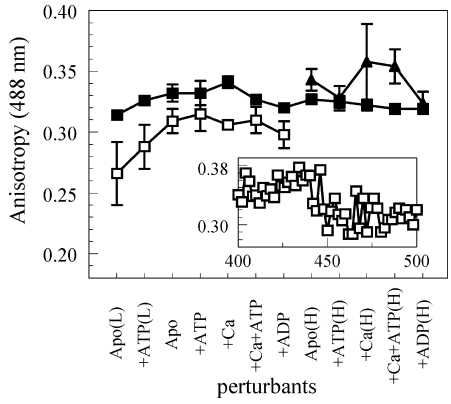

FIGURE 2: Polarization anisotropy for HCRLC-GFP in solution (■), HCRLC-PAGFP in solution (□), and HCRLC-GFP exchanged into full-length skeletal myosin (▲) vs conditions exactly imitating those for the fiber experiments with Apo∼Rigor, +ATP∼Relax, +ATP+Ca∼Active, +ADP∼ADP, and +ATP(L)∼low-μ Relax. A high ionic strength (H) implies addition of KPr or KCl to a final concentration of 0.5 M. Other in vitro conditions not duplicated in the fiber experiments are Apo(L) (low-μ Apo) and +Ca. Apo(L) is the +ATP(L) condition without ATP, and +Ca implies addition of 0.1 mM $CaCl_2$ to the Apo condition (normal or high ionic strength). Low- and high-ionic strength conditions correspond to ∼27 and 580 mM, respectively. All other conditions have an ionic strength of 150−160 mM. The inset shows the polarization anisotropy of HCRLC-PAGFP under Apo conditions over an excitation wavelength domain where the chromophore prior to photoactivation (un-photoactivated) and the photoactivated chromophore species absorb light (maxima at ∼410 and ∼488 nm, respectively). The sample giving the spectrum in the inset is a mixture of photoactivated and un-photoactivated molecules.

condition (low-μ Apo), where anisotropy is lower. HCRLC-PAGFP anisotropy is significantly lower than the HCRLC-GFP anisotropy. Polarization anisotropy from HCRLC-GFP exchanged into skeletal myosin (▲) varies within the standard deviation over conditions tested but at a somewhat higher level reflecting the slower rotational relaxation rate of the higher-molecular weight myosin−HCRLC-GFP complex.

Measurements on the exchanged full-length myosin system suggest that the GFP tag does not significantly change local or global rotational dynamics due to the presence of the perturbants. GFP and PAGFP have a common global structure (*41*), implying PAGFP identically interacts with the myosin host and likewise does not change global rotational dynamics due to perturbants. Measurements on HCRLC-GFP or HCRLC-PAGFP show the local or global rotational dynamics of the GFP or PAGFP tags are not affected by the perturbants, implying the chromophores maintain a similar orientation relative to the rotationally diffusing chimera under the conditions tested. Nonetheless, HCRLC-PAGFP anisotropy is lower than HCRLC-GFP anisotropy, probably reflecting local chromophore flexibility but not relative movement of PAGFP and HCRLC because GFP and PAGFP have a common global structure. The PAGFP chromophore is locally more flexible than GFP because it has a higher accessibility to quenchers (as observed here and in ref *42*) and because it must perform a large conformation change to accomplish photoactivation (*41*). The inset of Figure 2 shows polarization anisotropy from HCRLC-PAGFP under Apo conditions. The excitation wavelength domain includes contributions from both the photoactivated species (maximum absorption at ∼488 nm) and the chromophore species prior to photoactivation (un-photoactivated, with maximum absorption at ∼410 nm). The lower anisotropy in the photoactivated species probably reflects greater local flexibility in the photoactivated chromophore, although a larger angle between absorption and emission dipoles in this species will give the same result. The latter is unlikely because the chromophore itself is identical in the two species and because the absorption dipole peak absorption in the photoactivated species (488 nm) is red-shifted from the absorption dipole peak absorption in the un-photoactivated species (400 nm) but emission is from a common emission dipole. The anisotropy in the un-photoactivated species suggests highly aligned absorption and emission dipoles in the chromophore.

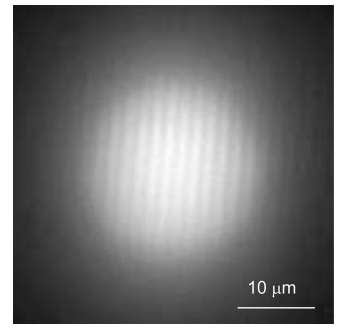

FIGURE 3: Fluorescence under 488 nm TIR illumination for densely photoactivated HCRLC-PAGFP in an exchanged fiber. Dense photoactivation was carried out with a brief exposure to 410 nm transmitted light. The brightly fluorescing circular disk corresponds to the region exposed to the 410 nm light. The pattern of light and dark bands within the disk originates from photoactivated PAGFPs on the myosin cross-bridges in the thick filaments.

Taken together, the polarization anisotropy measurements reflect the rotational mobility of the chromophore under the circumstances tested and suggest the local and global environment of the chromophore is not significantly affected by the perturbants when the HCRLC-PAGFP chimera occupies the RLC binding site on the myosin lever arm. The findings support the notion that changes in fluorescence polarization observed with the exchanged fiber (discussed next) reflect movement of the myosin lever arm. The noted exception, the low-ionic strength Apo condition, was not investigated in the exchanged fiber.

Work on permeabilized skeletal muscle fibers in which HCRLC-PAGFP is exchanged with the native RLC, discussed in Single HCRLC-PAGFP Detection in Exchanged Skeletal Muscle Fibers, will show that the chromophore maintains two discrete orientation populations relative to the fiber symmetry axis. The discrete orientation conformations are nearly equivalent in all physiological states of the fiber tested, while probabilities for occupation of a particular orientation conformation vary. These findings support the notion that the chromophore maintains a fixed orientation relative to the myosin lever arm because if it did otherwise observed orientation conformations would likewise change with physiological state.

Dense Photoactivation of HCRLC-PAGFP-Exchanged Skeletal Muscle Fibers. An exchanged muscle fiber with 60−70% of myosin heads containing HCRLC-PAGFP was exposed briefly to 410 nm transmitted light to densely photoactivate PAGFP. Figure 3 shows the photoactivated PAGFP fluorescence under 488 nm TIR illumination. The brightly fluorescing circular disk corresponds to the region

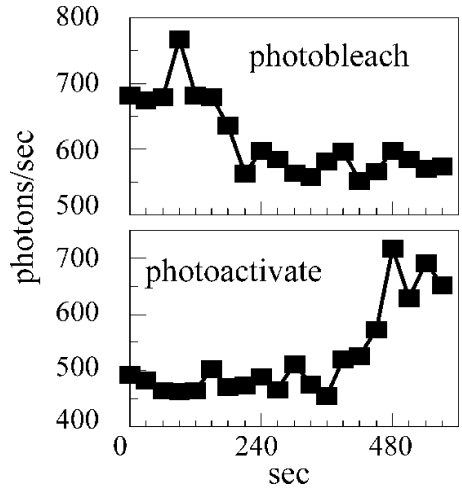

FIGURE 4: Photon counts from two different pixels as a function of time from a HCRLC-PAGFP-exchanged fiber. Intense and continuous TIR illumination at 488 nm photoactivated (bottom) and photobleached (top) PAGFP. Images were accumulated at 30 s intervals.

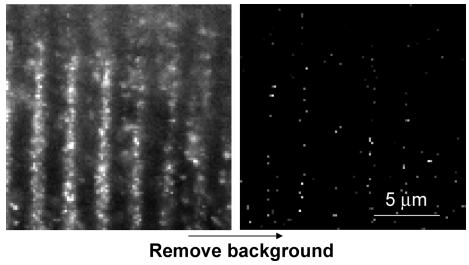

FIGURE 5: HCRLC-PAGFP-exchanged and sparsely photoactivated fiber in rigor under 488 nm TIR illumination for fluorescence observation of $F_{\|,\|}$. In the left panel, photoactivated PAGFPs are bright spots superimposed on the background fluorescence from un-photoactivated weakly fluorescing PAGFPs. The right panel is the same as the left panel except with the background removed.

exposed to the 410 nm light. The pattern of light and dark bands within the disk originates from photoactivated PAGFPs on the myosin cross-bridges in the thick filaments.

Single-HCRLC-PAGFP Detection in Exchanged Skeletal Muscle Fibers. Figure 4 shows photon counts from two different pixels as a function of time from a HCRLC-PAGFP-exchanged fiber. TIR illumination at 488 nm was continuous with intensity appropriate for PAGFP photoactivation rather than fluorescence excitation. Every 30 s an image was accumulated for 5 s (plotted counting rate adjusted to photos per second). The data show single-molecule photobleaching and photoactivation events where the intensity decreases and increases ~125 and ~200 counts, respectively. Background levels of ~575 or ~475 counts are from un-photoactivated PAGFP fluorescence. Other observed events produced increments as large as 400 counts, but the background level was also changing over time, making the implication appear less definitive. The events shown are typical and occurred frequently throughout the illuminated region. Activation events demonstrate that 488 nm light can photoactivate PAGFP. The 488 nm photoactivation of PAGFP under TIR illumination was used to produce all fiber images shown or analyzed subsequently.

Figure 5 shows a portion of a HCRLC-PAGFP-exchanged and sparsely photoactivated fiber in rigor under 488 nm TIR illumination for fluorescence observation. In the left panel,

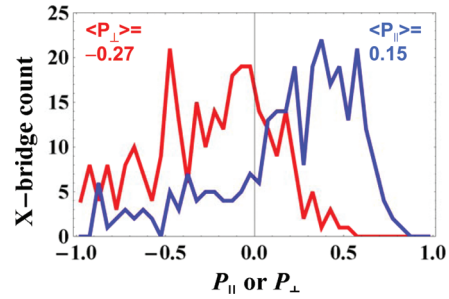

FIGURE 6: $P_{\|}$ (blue) and $P_{\perp}$ (red) histograms obtained by single-molecule measurements from ~300 HCRLC-PAGFP-tagged cross-bridges in one muscle fiber in rigor. Average polarization ratios for the histograms ($\langle P_i \rangle$) are indicated.

activated PAGFPs are bright spots superimposed on the background fluorescence from un-photoactivated weakly fluorescing PAGFPs. Photoactivated PAGFPs are apparently single molecules because their density in the fiber image implies an infinitesimal probability for two photoactivated molecules to reside in one pixel. Varied single-molecule intensities indicate varied proximity to the TIR surface where evanescent field intensity is maximal. Figure 5 shows $F_{\|,\|}$. An equivalent image for $F_{\|,\perp}$ is collected simultaneously using the DualView image splitter. The right panel is the same as the left panel except local average background has been removed as described in Materials and Methods.

Figure 6 shows $P_{\|}$ (blue) and $P_{\perp}$ (red) histograms obtained by single-molecule measurements from ~300 HCRLC-PAGFP-tagged cross-bridges in one muscle fiber in rigor. The average polarization ratios ($\langle P_i \rangle$) indicated in the figure show their wide divergence that is unique to single-molecule fluorescence polarization under TIRF. Figure 6 characterizes individual myosin lever arm orientations in situ.

Figure 7 shows single-molecule $P_{\|}$ histograms from fibers in rigor, in isometric contraction, in relaxation at normal and low μ, and in the presence of ADP. Data were gathered from parallel fiber samples in each physiological state. Histograms show evidence for two cross-bridge $P_{\|}$ subpopulations that are fitted with Gaussians drawn in the figure. The Gaussian distribution mean ($\langle P_{\|} \rangle$), width (σ), and occupation probability (p) for each fiber physiological state are summarized in Table 1. For the fiber states, distribution means are similar while widths vary somewhat more. Occupation probability is characteristic of each fiber state. Data in rigor and isometric contraction characterize the extent and direction of lever arm swing during the transition from the high-free energy state (subpopulation where $\langle P_{\|} \rangle \sim 0.46$ because this is predominant in isometric contraction) to the low-free energy state (subpopulation where $\langle P_{\|} \rangle \sim 0.19$ because this is predominant in rigor) in a native myosin as interpreted through the PAGFP dipole moment.

Figure 8 interprets $P_{\|}$ and $P_{\perp}$ in terms of probe dipole orientation as described in Materials and Methods. Left and right columns correspond to rigor and isometric contraction, respectively. The top two rows compare the single best-fitting simulated histogram (solid line) with observed (■) $P_{\|}$ and $P_{\perp}$ histograms. Excellent agreement between these quantities suggests successful modeling of the systems. The best-fit search includes the $P_{\|}$ and $P_{\perp}$ data sets simultaneously, while Gaussian curve fitting in Figure 7 included the $P_{\|}$ data set exclusively because the broader $P_{\perp}$ histogram does not distinguish the subpopulations by inspection.

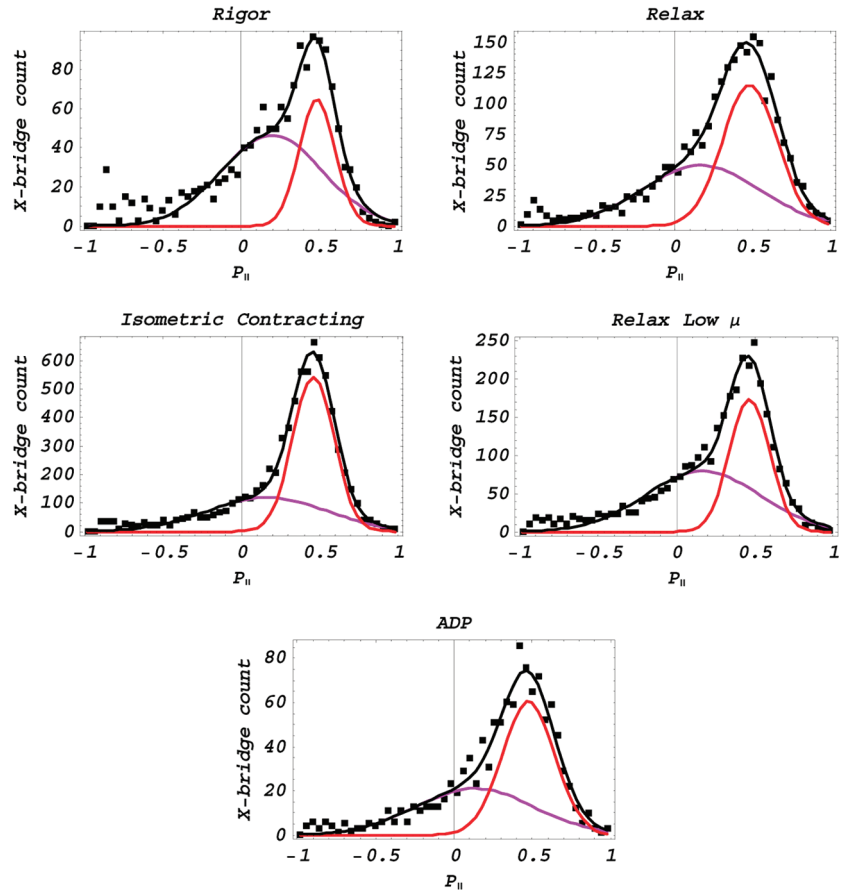

FIGURE 7: Single-molecule $P_{||}$ histograms from fibers in various physiological states. Data (■) are fitted (black line) by a sum of two Gaussian distributions (red or blue lines). Individual Gaussians give an average polarization ($\langle P_{||}\rangle$), distribution width [$\langle(\Delta P_{||})^2\rangle^{1/2}$], and occupation probability (p) for each fiber physiological state as summarized in Table 1.

Table 1: Tabulated and Simulated Results for $P_{||}$[a]

	single molecule					ensemble		
	total		Gaussian decomposition					
	$\langle P_{||}\rangle$	SD	$\langle P_{||}\rangle$	σ	p	$\langle P_{||}\rangle$	SD	SEM
rigor	0.204	0.39	0.484	0.11	0.32 ± 0.06	0.349	0.63	0.2 (N = 10)
			0.192	0.33	0.68			
isometric contraction	0.303	0.35	0.458	0.13	0.61 ± 0.04	0.433	0.80	0.16 (N = 24)
			0.162	0.38	0.39			
relax	0.295	0.36	0.480	0.18	0.52 ± 0.11	0.398	0.55	0.3 (N = 4)
			0.166	0.37	0.48			
low-μ relax	0.219	0.41	0.466	0.13	0.43 ± 0.04	0.366	0.65	0.2 (N = 12)
			0.166	0.37	0.57			
ADP	0.278	0.38	0.475	0.17	0.55 ± 0.14	0.368	0.62	0.4 (N = 3)
			0.133	0.37	0.45			
random	0.261	0.30	–	–	–	0.384	–	–

[a] Mean polarization ($\langle P_{||}\rangle$), standard deviation [SD or $\langle(\Delta P_{||})^2\rangle^{1/2}$], Gaussian width ($\sigma$), occupation probability (p), and standard deviation of the mean (SEM) observed from fibers in several physiological states. The random state is tabulated from 2543 simulated events. The total columns list $\langle P_{||}\rangle$ and SD from the histograms in Figure 7. The Gaussian decomposition columns list results from the same data decomposed into the two Gaussian distributions shown in Figure 7 with occupation probabilities proportional to the area under the Gaussian curves. Occupation probabilities sum to 1 for each physiological state and have standard error estimates from the nonlinear fitting routine in Mathematica (Wolfram Research, Champaign, IL). The ensemble columns list results from cases in which data from many chromophores were summed into total fluorescence intensities from a large region on the fiber and then polarization ratios were determined. The ensemble SD relates to experimental error and whole fiber variability but not to variability between single molecules. N in the last column is the number of independent measurements included in the tabulation of SEM.

PAGFPs on myosin cross-bridges have distributed β_0 and σ_β values shown by the histograms in the bottom row of Figure 8. The allowed choices shown correspond to 122 (left) and 253 (right) different probe distributions consistent with the F-ratio test as described in Materials and Methods. The distributed β_0 and σ_β values show the probe dipoles are probably not well characterized by a single Gaussian distribution in β; i.e., there are oriented subpopulations residing in the fiber. PAGFP dipoles are distributed in β_0 toward higher angles in rigor and lower angles in isometric contraction while $\sigma_\beta \sim 18-48°$. Partitioning the β_0 distribution into two portions at a β_0 of 20° finds fibers in rigor have 40 and 60% of cross-bridges in the $\beta_0 < \sim 20°$ and $\beta_0 > \sim 20°$ domains, respectively, while isometric contraction has a 65% to 35% split in correspondence with the occupation probabilities given in Table 1. PAGFPs on myosin cross-

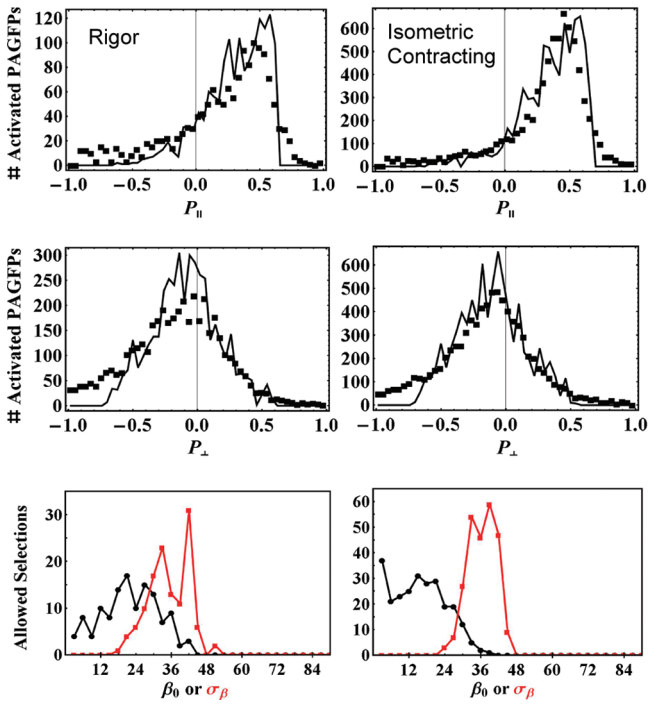

FIGURE 8: $P_{||}$ and $P_{\perp}$ histograms interpreted in terms of probe dipole orientation. Left and right columns correspond to rigor and isometric contraction, respectively. The top two rows compare best-fitting simulated (■) with observed (solid line) $P_{||}$ and $P_{\perp}$ histograms. The bottom row shows the selections best satisfying the constraints imposed by the measured data and allowed under the *F*-ratio test described in Materials and Methods for β_0 (black) and σ_β (red).

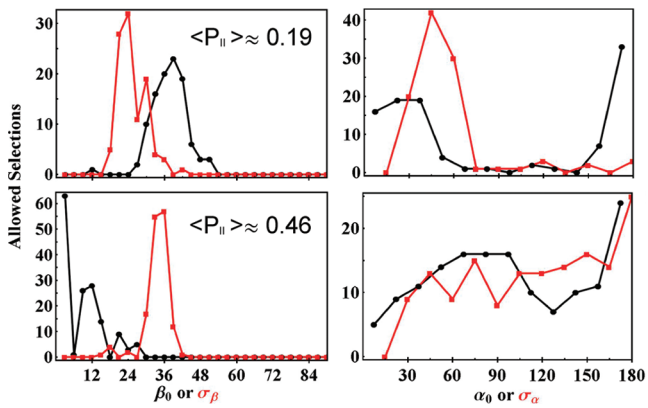

FIGURE 9: Best-fitting selections for β_0, α_0, σ_β, and σ_α with constraints from the Gaussian-distributed subpopulations identified in Figure 7 by the blue and red curves. All selections are allowed under the *F*-ratio test described in Materials and Methods. The top panels show allowed selections from the lower average polarization curve with $\langle P_{||} \rangle \approx 0.19$ predominant in the rigor fiber. The bottom panels show allowed selections from the higher average polarization with $\langle P_{||} \rangle \approx 0.46$ predominant in the isometric contracting fiber.

bridges are distributed evenly in α_0 and σ_α (data not shown). Although each cross-bridge binds at a distinct azimuthal coordinate, the ensemble has rotational symmetry about the fiber axis resulting in a flat distribution.

Figure 9 shows choices for β_0, α_0, σ_β, and σ_α giving the lowest χ^2 values for the Gaussian-distributed $P_{||}$ subpopulations identified in Figure 7 by the blue ($\langle P_{||} \rangle \approx 0.19$) or red ($\langle P_{||} \rangle \approx 0.46$) curves in rigor or isometric contraction and $P_{\perp}$ from the rigor or isometric contraction data in Figure 8 (middle panels). Choices correspond to 103 (top) or 149 (bottom) different probe distributions, consistent with the *F*-ratio test as described in Materials and Methods. The top

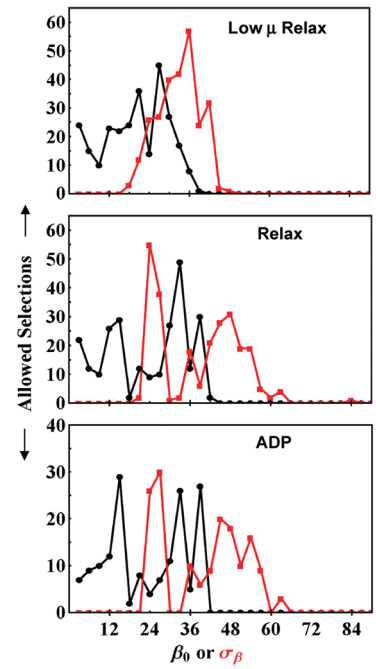

FIGURE 10: Best selections for average dipole orientation β_0 (black) and distribution width σ_β (red) satisfying constraints imposed by the measured $P_{||}$ and $P_{\perp}$ histograms for low-μ Relax, for Relax, and with ADP-bound fibers. All selections allowed under the *F*-ratio test are described in Materials and Methods.

panels in Figure 9 pertain to the lower average polarization curve predominant in the rigor fiber (Table 1) and correspond to $\langle \beta_0 \rangle \sim 38°$. The bottom panels in Figure 9 pertain to the higher average polarization curve predominant in the isometric contracting fiber (Table 1) and correspond to $\langle \beta_0 \rangle \sim 9°$. A transition between these subpopulations, which we propose as the force-producing transition in the cross-bridge, involves a complex change in all the angular degrees of freedom, including azimuthal and polar angles as well as the width of their respective distributions.

Figure 10 shows choices for β_0 (black) and σ_β (red) satisfying constraints imposed by the data measured in low-μ Relax, in Relax, and with ADP-bound conditions. The choices shown correspond to 265 (low-μ Relax), 252 (Relax), or 156 (ADP) different probe distributions, consistent with the *F*-ratio test as described in Materials and Methods.

The low-μ Relax condition has 47 and 53% of dipoles in the $\beta_0 < \sim 20°$ and $\beta_0 > \sim 20°$ domains, respectively; the Relax condition has 47 and 53% partitioning, respectively, and ADP has 44 and 56% partitioning, respectively. They are not significantly different from evenly partitioned dipoles.

DISCUSSION

Single-molecule characterization of protein conformation change elucidates the gamut of possibilities, including rare events that differ most from average behavior. The significance of characterizing rare events is well-recognized but rarely exploited in highly concentrated systems where it is technically difficult to isolate one molecule. Efficient fluorescence collection in a high-aperture microscope objective is ideally suited for single-chromophore detection, but visible confocal light microscopy has sufficient spatial resolution to separate signals from chromophores uniformly concentrated below ~6 nM. GFP-tagged protein components of cells

can be at a much higher concentration. This problem is addressed by increasing spatial resolution beyond the diffraction limit or by effectively lowering the chromophore concentration by sparsely photoactivation-enabling fluorescence from a few chromophores within the concentrated pool of un-photoactivated chromophores. The latter approach is the basis for PALM (*23*) and was used here to isolate light from single myosin cross-bridges in a muscle fiber. If the former approach is taken, far-field (*43, 44*) and near-field (*45, 46*) techniques have significantly reduced the detection volume from which fluorescence emission is collected.

We isolated emission from single molecules by sparse photoactivation of HCRLC-PAGFP exchanged onto the myosin lever arm in permeabilized muscle fibers. The application utilizes polarized fluorescence photoactivation and single-molecule detection to characterize myosin lever arm orientation in several muscle fiber physiological states. Single photoactivated molecule identification in a pixel containing many chromophores was a significant challenge because un-photoactivated probes fluoresce weakly, creating a substantial background. We devised a protocol for identifying single photoactivated PAGFPs based on a local background fluorescence estimate that eliminated with high certainty false identification of background light fluctuation with a photoactivated probe emission. Once a photoactivated probe is identified and its emission quantified, the reliable interpretation of polarized fluorescence requires that the probe be rigidly fixed to the host myosin lever arm. Polarized fluorescence spectroscopy suggested mobility of PAGFP on the tagged myosin lever arms is not affected by the chemical perturbants added to induce the various physiological states of the fiber. Thus, discrete polarization ratio subpopulations detected from the fiber reflect discrete lever arm orientation subpopulations. It also indicated that the photoactivated PAGFP species had a more mobile chromophore than an identically placed WT GFP probably due to local structural flexibility needed for photoactivateability.

Photoactivation with polarized TIR excitation introduced a photoactivated and photoselectively oriented set of chromophores to the exchanged HCRLC-PAGFP in muscle fibers. Photoselected activation (PsA) provides experimental control over probe specificity for different myosin lever arm rotational degrees of freedom in the fiber. Our experiments investigated two possibilities for PsA combined with passive observation of $P_{\parallel}$ and $P_{\perp}$. Here PsA and passive fluorescence excitation of chromophores were from identically polarized light so signals with the potential for the most intense emission could be detected. Crossed PsA and passive excitation polarizations, for instance, PsA with light polarized parallel to the fiber axis and fluorescence collected from excitation with light polarized perpendicular to the fiber axis, offer alternative excitation and detection schemes that will add meaningful, independent constraints to models of probe orientation dynamics in future experiments.

HCRLC-PAGFP exchanged onto myosin lever arms in a permeabilized muscle fiber indicated lever arm orientation populations in the fiber physiological states tested. Modeling the $P_{\parallel}$ single-molecule data with two Gaussian distributions (Figure 7) showed that the high average $P_{\parallel}$ population at 0.46−0.48 appears in every fiber state, which is clear by inspection. The lower average $P_{\parallel}$ population at 0.13−0.19 is not always apparent by inspection but was found with histogram fitting in all fiber states. The two $P_{\parallel}$ distributions relate to two narrow ranges of average polar angles (Figure 9) characterizing probe dipole orientation in the fiber. Occupation probability for the two Gaussians (Table 1) distinguishes cross-bridge deployment in each of the fiber states tested. We assign M and M** myosin conformations (straight and bent, respectively) to the two Gaussians based on independent knowledge of the S1 crystal structures. S1 occupies these conformations without actin, and we assume there is an approximate correspondence to the straight and bent forms when S1 is bound to actin.

Contraction initiation from the rigor state is a shift in the cross-bridge lever arm preference from one to the other orientation distribution that we propose corresponds to a shift from the straight to bent conformation, respectively. The straight conformation associates with the rigor state in a fiber and the Apo skeletal myosin crystal structure 2mys (*13*). The bent conformation associates with the active state in a fiber and the M** smooth muscle myosin crystal structure 1br1 (*6*). Hence, our results relating the polarization ratios to probe dipole orientation (Figures 8 and 10) suggest the straight or bent conformations are associated with the $\beta_0 > \sim 20°$ or $\beta_0 < \sim 20°$ PAGFP chromophore orientation, respectively. All fiber physiological states contain straight and bent cross-bridges, but their deployment into these conformations differs among states.

Evenly distributed (50:50) straight and bent cross-bridge subpopulations persist when interaction with actin is negligible, suggesting the myosin filament prepositions the head moiety for favorable interaction with actin. Unbound native cross-bridges are oriented by the thick filament with ionic interactions (*47*). The actin interaction is responsible for shifting the occupation probability from the 50:50 mixture. PAGFP−PAGFP interactions, on the same or adjacent myosin molecules, could affect chromophore orientation. Previous work at low GFP tagged MLC concentrations, when interaction between GFPs is improbable, also showed similar cross-bridge subpopulations, suggesting our observation is unlikely to be caused by interacting PAGFPs. Nevertheless, future work should investigate potential mutual probe interactions by titrating exchanged HCRLC-PAGFP using a mixture of tagged and untagged light chain.

Crowded conditions could influence conformation incrementally, but similar straight and bent cross-bridge conformations appear under each fiber condition tested. Instead, crowding probably alters the occupation probability of the stable conformations like nucleotide binding in the active site. Previously, we accomplished single-molecule detection in HCRLC-GFP-exchanged rigor fibers at the A-band periphery where the cross-bridge concentration is low and observed both the $\beta_0 > \sim 20°$ and $\beta_0 < \sim 20°$ lever arm orientation states with the lower angle state predominant. Ensemble experiments with HCRLC-GFP within the A-band where cross-bridge concentration is extremely high (except at the M-line borders where the cross-bridge is excluded) indicated the predominant greater than ∼20° lever arm orientation but failed to detect the minor component with a less than ∼20° lever arm orientation. Single-molecule experiments on the whole A-band presented here indicate both $\beta_0 > \sim 20°$ and $\beta_0 < \sim 20°$ lever arm orientation states with the higher angle state predominant. Whole A-band experiments sample highly concentrated myosin preferen-

tially due to the concentration weighting. Molecular crowding within the A-band apparently shifts the predominant conformation to the straight form. Although consistent with the previous work from the exchanged HCRLC-GFP rigor fibers, the new single-molecule data provide the clearest indication of the crowding effect on myosin conformation. An important research objective is to definitively correlate the lever arm orientation ($\beta_0 > \sim 20°$ or $\beta_0 < \sim 20°$) with the straight or bent myosin cross-bridge conformation.

Inhomogeneity in thick filament structure might be ultimately responsible for observed differences in cross-bridge orientation along the thick filament. Oshima et al. suggested that myosin filament conformation has regular and perturbed regions corresponding approximately to the edge and central part of the thick filament (*48*). These observations parallel ours using the fluorescent probe-tagged MLC, suggesting both are indicative of the same crowding phenomena.

The results suggest we view muscle shortening during contraction as free energy-driven rebalancing of cross-bridge population from the bent to straight conformation due to the favorable conformation free energy change accompanying product release plus the effect of molecular crowding. ATP hydrolysis at the active site is the free energy source promoting the actin-detached cross-bridge into the bent conformation against the conformational free energy gradient. We have shown previously that nucleotide-bound myosin in the presence of a crowding cosolvent is trapped in the bent conformation probably because of its lower surface area (*28*). This preference enhances the free energy balance for lever arm repriming but must reverse for the Apo actomyosin state since the straight conformation is predominant in the rigor fiber. The reversal could be due to actin binding and/or actin binding cleft closure. Actin binding is required for force generation, and Apo actomyosin favors the straight conformation at the power stroke completion, giving the cross-bridge additional free energy (aside from that derived from the conformational free energy change accompanying product release) to utilize just when it is needed during force production.

The relaxed, low-μ relaxed, and ADP states all have nucleotide bound to the cross-bridge, and all maintain even distributions of bent and straight conformations (Table 1). Previous results suggest crowding should stabilize the bent conformation (*28*); however, association with actin in the low-ionic strength relaxed and ADP states moves the equilibrium toward the straight conformation as it does for rigor. The relaxed cross-bridge is usually not actin-attached; hence, its polarized fluorescence is an unreliable indicator of lever arm conformation because the parent population from which subpopulations are formed is more disordered. The relaxed cross-bridge is also highly dynamic, somewhat complicating interpretation of occupation probability (as remarked in Materials and Methods). The even distribution of bent and straight conformations in ADP suggests some of the boost to the free energy of contraction contributed by crowding occurs with ADP release.

CONCLUSIONS

A single myosin cross-bridge orientation was detected within the A-band where the myosin concentration exceeds 100 μM from muscle fibers in several physiological states. Isolation of the individual molecules for observation was accomplished using a photoactivatable probe-tagged myosin light chain exchanged into permeabilized skeletal muscle fibers. The exchanged HCRLC-PAGFP labeled the myosin lever arm and was sparsely photoactivated using polarized light. Photoselective activation and collection of polarized fluorescence enabled evaluation of the lever arm orientation changes. Two lever arm orientation populations, straight and bent, have varying occupation probabilities characterizing all physiological states. Contraction initiation from the rigor state is a shift in the cross-bridge preference from the straight to the bent form. Previous single-molecule detection of lever arm orientation at the A-band periphery where the cross-bridge concentration is low likewise indicated the straight and bent conformations with the bent form predominant in rigor. Experiments here on the whole A-band indicate the straight form predominates in rigor. Molecular crowding within the A-band apparently shifts the predominant conformation from the bent to the straight form. The latter could have a role in contraction because it provides free energy to the cross-bridge during force production in addition to that derived from the conformation free energy change accompanying product release.

ACKNOWLEDGMENT

We gratefully acknowledge Dr. D. Szczesna-Cordary for the generous gift of the HCRLC cDNA and Miriam F. Halstead for technical advice.

SUPPORTING INFORMATION AVAILABLE

Fluorescence from HCRLC-GFP-exchanged fibers indicates localization of GFP to the myosin thick filament. This material is available free of charge via the Internet at http://pubs.acs.org.

REFERENCES

1. Huxley, H. E. (1969) The mechanism of muscular contraction. *Science 164*, 1356–1366.
2. Onishi, H., and Morales, M. F. (2007) A closer look at energy transduction in muscle. *Proc. Natl. Acad. Sci. U.S.A. 104*, 12714–12719.
3. Peyser, Y. M., Ajtai, K., Werber, M. M., Burghardt, T. P., and Muhlrad, A. (1997) Effect of metal cations on the conformation of myosin subfragment-1-ADP-phosphate analog complexes: A near UV circular dichroism study. *Biochemistry 36*, 5170–5178.
4. Trentham, D. R., Eccleston, J. F., and Bagshaw, C. R. (1976) Kinetic analysis of ATPase mechanisms. *Q. Rev. Biophys. 9*, 217–281.
5. Marston, S. B., and Taylor, E. W. (1980) Comparison of the myosin and actomyosin ATPase mechanisms of the four types of vertebrate muscles. *J. Mol. Biol. 139*, 573–600.
6. Dominguez, R., Freyzon, Y., Trybus, K. M., and Cohen, C. (1998) Crystal structure of a vertebrate smooth muscle myosin motor domain and its complex with the essential light chain: Visualization of the pre-power stroke state. *Cell 94*, 559–571.
7. Highsmith, S. (1999) Lever arm model of force generation by actin-myosin-ATP. *Biochemistry 38*, 9792–9797.
8. Geeves, M. A., and Holmes, K. C. (1999) Structural mechanism of muscle contraction. *Annu. Rev. Biochem. 68*, 687–728.
9. Highsmith, S., and Eden, D. (1993) Myosin-ATP chemomechanics. *Biochemistry 32*, 2455–2458.
10. Wakabayashi, K., Tokunaga, M., Kohno, I., Sugimoto, Y., Hamanaka, T., Takezawa, Y., Wakabayashi, T., and Amemiya, Y. (1992) Small-angle synchrotron X-ray scattering reveals distinct shape changes of the myosin head during hydrolysis of ATP. *Science 258*, 443–447.

11. Aguirre, R., Lin, S. H., Gonsoulin, F., Wang, C. K., and Cheung, H. C. (1989) Characterization of the ethenoadenosine diphosphate binding site of myosin subfragment 1. Energetics of the equilibrium between two states of nucleotide-S1 and vanadate-induced global conformation changes detected by energy transfer. *Biochemistry 28*, 799–807.
12. Uyeda, T. Q. P., Abramson, P. D., and Spudich, J. A. (1996) The neck region of the myosin motor domain acts as a lever arm to generate movement. *Proc. Natl. Acad. Sci. U.S.A. 93*, 4459–4464.
13. Rayment, I., Rypniewski, W. R., Schmidt-Base, K., Smith, R., Tomchick, D. R., Benning, M. M., Winkelmann, D. A., Wesenberg, G., and Holden, H. M. (1993) Three-dimensional structure of myosin subfragment-1: A molecular motor. *Science 261*, 50–58.
14. Wagner, P. D., and Weeds, A. G. (1977) Studies on the role of myosin alkali light chains. Recombination and hybridization of light chains and heavy chains in subfragment one preparations. *J. Mol. Biol. 109*, 455–470.
15. Arata, T. (1990) Orientation of spin-labeled light chain 2 of myosin heads in muscle fibers. *J. Mol. Biol. 214*, 471–478.
16. Irving, M., Allen, T. S. C., Sabido-David, C., Cralk, J. S., Brandmeler, B., Kendrick-Jones, J., Corrie, J. E. T., Trentham, D. R., and Goldman, Y. E. (1995) Tilting of the light-chain region of myosin during step length changes and active force generation in skeletal muscle. *Nature 375*, 688–690.
17. Borejdo, J., Ushakov, D. S., and Akopova, I. (2002) Regulatory and essential light chains of myosin rotate equally during contraction of skeletal muscle. *Biophys. J. 82*, 3150–3159.
18. Burghardt, T. P., Ajtai, K., Chan, D. K., Halstead, M. F., Li, J., and Zheng, Y. (2007) GFP Tagged Regulatory Light Chain Monitors Single Myosin Lever-Arm Orientation in a Muscle Fiber. *Biophys. J. 93*, 2226–2239.
19. Grey, C., Méry, A., and Pucéat, M. (2005) Fine-tuning in Ca^{2+} homeostasis underlies progression of cardiomyopathy in myocytes derived from genetically modified embryonic stem cells. *Hum. Mol. Genet. 14*, 1367–1377.
20. Chalfie, M., Tu, Y., Euskirchen, G., Ward, W. W., and Prasher, D. C. (1994) Green fluorescent protein as a marker for gene expression. *Science 263*, 802–805.
21. Brejc, K., Sixma, T. K., Kitts, P. A., Kain, S. R., Tsien, R. Y., Ormo, M., and Remington, S. J. (1997) Structural basis for dual excitation and photoisomerization of the *Aequorea victoria* green fluorescent protein. *Proc. Natl. Acad. Sci. U.S.A. 94*, 2306–2311.
22. Patterson, G. H., and Lippincott-Schwartz, J. (2002) A photoactivatable GFP for selective photolabeling of proteins and cells. *Science 297*, 1873–1877.
23. Betzig, E., Patterson, G. H., Sougrat, R., Lindwasser, O. W., Olenych, S., Bonifacino, J. S., Davidson, M. W., Lippincott-Schwartz, J., and Hess, H. F. (2006) Imaging intracellular fluorescent proteins at nanometer resolution. *Science 313*, 1642–1645.
24. Hess, S. T., Girirajan, T. P. K., and Mason, M. D. (2007) Ultra-high resolution imaging by fluorescence photoactivation localization microscopy. *Biophys. J. 91*, 4258–4272.
25. Rust, M. J., Bates, M., and Zhuang, X. (2006) Sub-drffraction-limit imaging by stochastic optical reconstruction microscopy (STORM). *Nat. Methods 3*, 793–795.
26. Neuweiler, H., and Sauer, M. (2005) Exploring life by single-molecule fluorescence spectroscopy. *Anal. Chem. 77*, 179A–185A.
27. Minton, A. P. (2001) The influence of macromolecular crowding and macromolecular confinement on biochemical reactions in physiological media. *J. Biol. Chem. 276*, 10577–10580.
28. Peyser, Y. M., Shaya, S., Ajtai, K., Burghardt, T. P., and Muhlrad, A. (2003) Cosolvent induced aggregation inhibits myosin ATPase activity by stabilizing the predominant transition intermediate. *Biochemistry 42*, 12669–12675.
29. Bagshaw, C. R. (1982) in *Outline Studies of Biology: Muscle Contraction*, p 22, Chapman and Hall, London.
30. Tikunov, B. A., Sweeney, H. L., and Rome, L. C. (2001) Quantitative electrophoretic analysis of myosin heavy chains in single muscle fibers. *J. Appl. Physiol. 90*, 1927–1935.
31. Szczesna, D., Ghosh, D., Li, Q., Gomes, A. V., Guzman, G., Arana, C., Zhi, G., Stull, J. T., and Potter, J. D. (2001) Familial hypertrophic cardiomyopathy mutations in the regulatory light chains of myosin affect their structure, Ca^{2+} binding, and phosphorylation. *J. Biol. Chem. 276*, 7086–7092.
32. Borejdo, J., Putnam, S., and Morales, M. F. (1979) Fluctuations in polarized fluorescence: Evidence that muscle cross bridges rotate repetitively during contraction. *Proc. Natl. Acad. Sci. U.S.A. 76*, 6346–6350.
33. Brack, A. S., Brandmeier, B., Ferguson, R. E., Criddle, S., Dale, R., and Irving, M. (2004) Bifunctional rhodamine probes of myosin regulatory light chain orientation in relaxed skeletal muscle fibers. *Biophys. J. 86*, 2329–2341.
34. Yang, Z., and Sweeney, H. L. (1995) Restoration of phosphorylation-dependent regulation to the skeletal myosin regulatory light chain. *J. Biol. Chem. 270*, 24646–24649.
35. Axelrod, D., and Omann, G. M. (2006) Combinatorial microscopy. *Nat. Rev. Mol. Cell Biol. 7*, 944–952.
36. Burghardt, T. P., and Thompson, N. L. (1984) Evanescent intensity of a focused gaussian light beam undergoing total internal reflection in a prism. *Opt. Eng. (Bellingham, WA, U.S.) 23*, 62–67.
37. Burghardt, T. P., Ajtai, K., and Borejdo, J. (2006) In situ single molecule imaging with attoliter detection using objective total internal reflection confocal microscopy. *Biochemistry 45*, 4058–4068.
38. Hellen, E. H., and Axelrod, D. (1987) Fluorescence emission at dielectric and metal-film interfaces. *J. Opt. Soc. Am. B 4*, 337–350.
39. Thompson, N. L., and Burghardt, T. P. (1986) Total-internal reflection fluorescence: Measurement of spatial and orientational distributions of fluorophores near planar dielectric interfaces. *Biophys. Chem. 25*, 91–97.
40. Axelrod, D. (1979) Carbocyanine dye orientation in red cell membrane studied by microscopic fluorescence polarization. *Biophys. J. 26*, 557–573.
41. Henderson, J. N., Ai, H., Campbell, R. E., and Remington, S. J. (2007) Structural basis for reversible photobleaching of a green fluorescent protein homologue. *Proc. Natl. Acad. Sci. U.S.A. 104*, 6672–6677.
42. Arosio, D., Garau, G., Ricci, F., Marchetti, L., Bizzarri, R., Nifosi, R., and Beltram, F. (2007) Spectroscopic and structural study of proton and halide ion cooperative binding to GFP. *Biophys. J. 93*, 232–244.
43. Donnert, G., Keller, J., Medda, R., Andrei, M. A., Rizzoli, S. O., Luhrmann, R., Jan, R., Eggeling, C., and Hell, S. W. (2006) Macromollecular-scale resolution in biological fluorescence microscopy. *Proc. Natl. Acad. Sci. U.S.A. 103*, 11440–11445.
44. Shao, L., Isaac, B., Uzawa, S., Agard, D. A., Sedat, J. W., and Gustafsson, M. G. L. (2008) I5S: Wide-Field Light Microscopy with 100-nm-Scale Resolution in Three Dimensions. *Biophys. J. 94*, 4971–4983.
45. Ruckstuhl, T., and Seeger, S. (2004) Attoliter detection volumes by confocal total-internal-reflection fluorescence microscopy. *Opt. Lett. 29*, 569–571.
46. Burghardt, T. P., Charlesworth, J. E., Halstead, M. F., Tarara, J. E., and Ajtai, K. (2006) In situ fluorescent protein imaging with metal film-enhanced total internal reflection microscopy. *Biophys. J. 90*, 4662–4671.
47. Burghardt, T. P., Tidswell, M., and Borejdo, J. (1984) Cross-bridge order and orientation in resting single glycerinated muscle fibers studied by linear dichroism of bound rhodamine labels. *J. Muscle Res. Cell Motil. 5*, 657–663.
48. Oshima, K., Takezawa, Y., Sugimoto, Y., Kobayashi, T., Irving, T. C., and Wakabayashi, K. (2007) Axial Dispositions and Conformations of Myosin Crossbridges Along Thick Filaments in Relaxed and Contracting States of Vertebrate Striated Muscles by X-ray Fiber Diffraction. *J. Mol. Biol. 367*, 275–301.

BI8017703